Particuology 115 (2026) 277–291

Contents lists available at ScienceDirect

Particuology

journal homepage: www.elsevier.com/locate/partic

# Transport mechanism of proppants in complex fracture networks based on multiphase particle-in-cell method

Qiang Wang[a,1], Yufeng Wang[a,1,*], Jinzhou Zhao[a], Hai Liu[b], Hao Gao[c,d], Yuchao Zhou[a], Yongquan Hu[a]

[a] State Key Laboratory of Oil and Gas Reservoir Geology and Exploitation, Southwest Petroleum University, Chengdu, China
[b] No. 11 Oil Production Plant, Changqing Oilfield Company, Qinyang, China
[c] Oil and Gas Technology Research Institute, PetroChina Changqing Oilfield Company, Xi'an, China
[d] National Engineering Laboratory for Exploration and Development of Low Permeability Oil & Gas Fields, Xi'an, China

## HIGHLIGHTS

- MP-PIC model couples realistic shale geometries for complex fracture networks.
- Early-stage vortexes and high injection rates aggravate placement heterogeneity.
- Dual proppant transport mechanisms emerge across Main and Secondary fractures.
- Proppant volume decays distally; large intersection angles hinder migration.
- Reducing proppant density/size and elevating viscosity enhance sweep efficiency.

## GRAPHICAL ABSTRACT

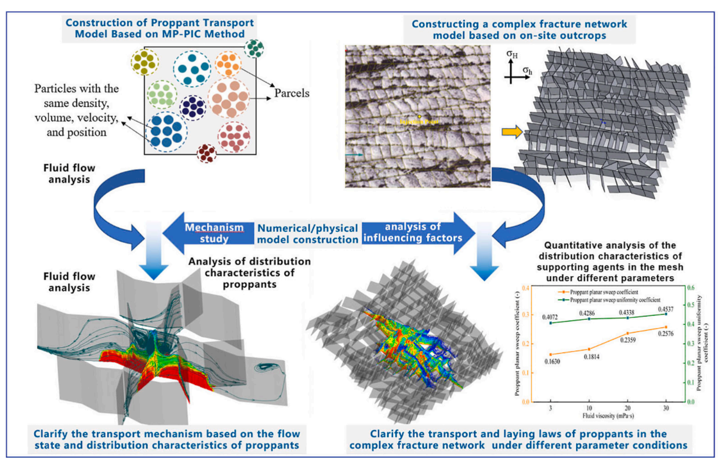


## ARTICLE INFO

*Keywords:*
Multiphase particle-in-cell method
Liquid-solid two-phase flow
Eulerian-Lagrangian method
Complex fracture network
Proppant transport

## ABSTRACT

To improve understanding of proppant transport mechanisms in complex fracture networks, a field-scale model based on the Multiphase Particle-in-Cell (MP-PIC) method was developed using fracture geometries derived from real shale outcrops and validated against experimental data. Results indicate that: (1) intense vortex formation during early-to-mid injection stages or at high flow rates exacerbates the longitudinal heterogeneity of proppant distribution. (2) In the near-wellbore zone, the synergistic effects of fracture width variations, high flow velocities, and natural weak planes drive proppants to migrate preferentially along paths aligned with the maximum and minimum principal stress directions, forming a dual-channel transport pattern. (3) The volume of proppant entering secondary fractures decreases with distance from the injection point, and the proppant dune height within dominant channels exhibits stepwise attenuation. Larger intersection angles between secondary

* Corresponding author.
*E-mail address:* 202515000006@stu.swpu.edu.cn (Y. Wang).
[1] These authors contributed equally to this work.

https://doi.org/10.1016/j.partic.2026.05.021
Received 2 March 2026; Received in revised form 19 May 2026; Accepted 29 May 2026
Available online 6 June 2026

and main fractures hinder proppant migration. (4) Smaller proppant size and lower density improve the planar sweep and distribution uniformity coefficients, while increased fracturing fluid viscosity extends the proppant sweep range and further improves uniformity; high injection rates promote long-distance proppant transport and broader coverage but may reduce uniformity, leading to sparse proppant distribution and necking at fracture mouths. These findings provide quantitative guidance for optimizing hydraulic fracturing designs.

## 1. Introduction

Hydraulic fracturing is a pivotal technique for the development of unconventional oil and gas resources, with shale gas serving as a prime example. High-volume proppant fracturing is widely employed to achieve commercial viability in these reservoirs. This technology inherently comprises two coupled processes: high-pressure fluid injection to initiate and propagate fractures, and the subsequent transport and placement of proppants to mechanically sustain the created fracture aperture (He et al., 2021; Ma & Xie, 2018; Zhao et al., 2024). The former establishes the necessary conduits, while the latter prevents fracture closure, thereby creating highly conductive flow paths for hydrocarbon extraction. The synergy between these processes is paramount for ensuring optimal fracturing efficacy. Despite its widespread application, significant engineering challenges persist, largely stemming from the complex geological characteristics of shale reservoirs. The activation of natural weak planes during the fluid injection stage frequently generates highly intricate fracture networks (Hu et al., 2021, 2025; Wang et al., 2024a, 2025; Wang et al., 2024b; Zhou et al., 2026), which significantly complicates the subsequent proppant transport. Because effective proppant placement directly dictates the ultimate fracture conductivity—a primary determinant of hydraulic fracturing success—a comprehensive understanding of proppant transport dynamics within these complex networks is indispensable. However, existing research in this domain remains insufficient, and field-scale fracturing designs often lack robust scientific guidelines, particularly concerning the optimization of injection rates, proppant selection, and overall treatment scale. Consequently, developing realistic fracture network models and conducting targeted investigations into proppant transport mechanisms are of critical importance.

To elucidate the transport behaviors and placement mechanisms of proppants within hydraulic fractures, extensive research has been conducted through both laboratory experiments and numerical simulations (Yao et al., 2022), as summarized in Table 1.

Most studies on proppant transport have traditionally relied on laboratory experiments with simplified setups to investigate variables like proppant properties and fracture width (Clark & Guler, 1983; Daniel & Ingrid, 2019; Denney, 2010; Qu et al., 2022; Sahai et al., 2014; Bahri & Miskimins, 2021). Despite providing foundational insights, these laboratory models often struggle to replicate the intricacies of complex fracture networks due to scale limitations. To overcome these constraints, scholars have increasingly turned to numerical simulations. Early numerical efforts, such as the finite difference approach by Cleary et al. (1993), identified that proppant bridging and plugging are highly localized at fracture intersections, which can be mitigated by alternating slurry concentrations. Subsequent 3D CFD and Euler–Euler modeling has further elucidated the extreme sensitivity of settling patterns and two-phase flow dynamics to fluid velocity and proppant density (Tsai et al., 2013; Zhang et al., 2014). By integrating discrete phase modeling with experimental data, researchers like Tong and Mohanty (2016) and Han et al. (2016) have characterized the stratified flow regions within fractures and the sensitivity of proppant-packed layers to fluid pressure. Hou et al. (2022) combined experiments with deep learning to investigate alternating slurry injection at the field scale, showing that it induces proppant ridge formation, with the pump rate being the key factor influencing ridge height.

As actual reservoir fractures are typically multi-branched rather than idealized, research has increasingly pivoted toward multi-stage systems. Li et al. (2017) found that increasing the branching angle makes slurry entry into branches significantly more difficult, thereby reducing sand bed height. Following this, Kong and McAndrew (2017) developed a Euler-Euler multiphase flow model via CFD, identifying fracture width, fluid viscosity, and sand load as the primary drivers of proppant distribution. Focusing specifically on microscopic transport mechanisms, Yang et al. (2019) introduced a Euler multiphase model for small-scale fracture network simulations. To address even higher structural complexity, Zeng et al. (2022) developed a numerical model using the Euler-Lagrange method for a three-tier fracture system, specifically examining operational factors. Zhao et al. (2024) conducted CFD simulations, which revealed that proppants tend to settle at the mouth of the main fracture, with smaller branching angles facilitating entry into the network.

Despite these efforts, many models still rely on simplified planar geometries or regular network patterns, often overlooking the curved trajectories and structural weak planes inherent in shale reservoirs (Yu et al., 2019). These irregular features directly dictate placement efficiency in non-planar fractures. To address this, Gong et al. (2020) incorporated fracture non-planarity and surface roughness into a CFD model, demonstrating that rough surfaces significantly impede transport velocity. Nilzon and Hu (2023) further applied the kinetic theory of granular flow (KTGF) to study curved fractures, emphasizing the coupled effects of diameter and fluid viscosity. However, even these advanced representations remain largely confined to small-scale domains. There remains a critical need for models that can fully capture proppant transport behaviors at the true field scale without sacrificing the complexity of real fracture geometries.

In summary, traditional CFD-DEM methods are limited by the immense computational cost at the particle level, making large-scale simulations difficult, while Eulerian-Lagrangian methods have inherent limitations in handling irregular boundaries and high-concentration particle collisions. Although previous MP-PIC studies have improved computational efficiency, most remain confined to simplified micro- or experimental-scale geometric models. This study aims to specifically overcome three core limitations of previous research by: (1) discarding conventional orthogonal or regular models and directly constructing a physical fracture network model based on high-definition images of real shale outcrops; (2) preserving the curvature and bending characteristics of real fracture surfaces during meshing to investigate the disturbances caused by actual wall morphologies on the flow field and proppants; and (3) breaking through the computational cost bottleneck to successfully expand the multiphase flow computational domain to the field scale, thereby meeting the engineering requirements for high-precision and low-cost simulation of proppant transport.

To this end, this paper applies a three-dimensional MP-PIC (Multiphase Particle-in-Cell) model to complex large-scale problems and introduces two evaluation indices, the proppant planar sweep efficiency and the planar sweep uniformity coefficient, achieving efficient simulation of the entire process of proppant transport, settlement, and accumulation in field-scale fracture networks. Specifically, first, taking real rock outcrops as a reference, the complex geometric morphology of the fracture network is finely delineated using real rock outcrops as a reference. Second, a localized small-scale fracture network model is selected from the complex physical model to focus on the dispersion and accumulation characteristics of proppants within the main fractures, bedding fractures, and secondary fractures, thereby revealing the

**Table 1**
Literature review of proppant transport simulation.

| Literature | Method | Fracture type | Scale | Injection rate | Research parameters |
|---|---|---|---|---|---|
| Han et al. (2016) | Computational fluid dynamics (CFD) model | Multi secondary fractures | 65.6 ft × 39.4 ft × 0.02 ft | 54 bbl/min | Fluid viscosity; Proppant density; Injection rates; Proppant diameter |
| Tong and Mohanty (2016) | Hybrid Eulerian-Lagrangian model, and Dense Discrete Phase Model (DDPM) | Multi secondary fractures | 0.381 m × 0.0762 m × 0.002 m | 0.1-0.3 m/s | Shear rate; Bypass angle; Sand size |
| Li et al. (2017) | Plexiglas plate fracture model, and ANSYS Fluent software | Multi secondary fractures | 2 m × 1 m × 0.004 m | 0.3-0.6 $m^3$/h | Proppant diameter; Sand ratios; Injection rate; Secondary-fracture angle |
| Kong and McAndrew (2017) | CFD method based on Euler- Euler Model | Multi secondary fractures | 10 m × 2.7 m × 0.006 m | 3-6 m/s | Fracture shapes; Fluid viscosity; Fracture width; Proppant size; Proppant density; Proppant load; Injection rate |
| Hu et al. (2018) | Eulerian-Eulerian model | Single straight fracture | 100 m × 40 m × 0.002 m | 0.013-0.065 $m^3$/s | Fluid viscosity; Proppant injection rate; Fracture height; Proppant concentration |
| Roostaei et al. (2018) | Eulerrian-Lagrange model | Fixed rectangular and elliptical fractures | 5 m × 5 m × 0.003 mm | 1.325 lit/s | Proppant diameter; Fluid viscosity; Elliptical slot; Buoyancy number |
| Zeng et al. (2019) | 2D Eulerian-Lagrangian framework based on MP-PIC method | Single straight fracture | 300 m × 25 m × 0.002 m | 0.5 $m^3$/min | Proppant density; Proppant diameter; Fluid viscosity; Fluid flow rate |
| Yang et al. (2019) | Eulerian multiphase model | Complex fracture network | 2 m × 0.6 m × 0.006 m | 0.6-1 m/s | Proppant density; Proppant diameter; Proppant concentration; Fracture types |
| Siddhamshetty et al. (2020) | 3D MP-PIC model | Single straight fracture | 180 m × 30 m × 0.00762 m | 10 bbl/min | Proppant diameter; Injection time |
| Gong et al. (2020) | CFD method based on Euler-Euler model | Multi secondary fractures | 9.1 m × 6.1 m × 0.003 m | 3 m/s | Fracture geometry; Surface roughness; Secondary and tertiary fracture angle |
| Xiao et al. (2021) | Visual tablet model | Multi secondary fractures | 4 m × 0.5 m × 0.006 m | 1-4 $m^3$/h | Pumping rate; Fluid viscosity; Proppant diameter; Proppant concentration; Secondary-fracture angle; Injection time |
| Qu et al. (2021) | Acrylic sheet model | Nonplanar fracture with bends | 1.5 m × 0.27 m × 0.004 m | 0.21-0.42 m/s | Particle size; Particle density; Offset section; Fluid velocity; Particle types Injection time |
| Tatman et al. (2022) | DLP technology to 3D print fracture networks | Multi secondary fractures | 4 ft ×22 in ×0.198 in | 15 gal/min | Proppant diameter; Secondary fracture location |
| Zeng et al. (2022) | CFD method based on Euler-Lagrange model | Multi secondary fractures | 1.2 m × 0.3 m× 0.006 m | 0.2-0.4 m/s | Injection rate; Proppant concentration; Fluid viscosity; Proppant size; Fracture width |
| Zhou et al. (2023) | Two fluid method | Rough single fracture | 4 m × 0.3 m×0.01 m | 10 L/min | Fracture morphology; Fracture aperture; Fracture mated state |
| Nilzon and Hu (2023) | Hybrid CFD model combined with the kinetic theory of granular flow (KTGF) | Complex fracture network | 2 m × 0.0762 m× 0.002 m | 0.1-0.5 m/s | Proppant diameter; Fluid velocity Fluid viscosity |
| Li, (2024); Li et al. (2024) | CFD-DEM coupling method | Tortuous single fracture | 0.2 m × 0.1 m × 0.009 m | 0.4 m/s | Fracture type; Inclination angle; Injection velocity; Proppant density; Proppant radius; Fracture width; Proppant concentration |
| Zhao et al. (2024) | CFD method based on Euler- Euler model | Multi secondary fractures | 4 m × 0.16 m × 0.004 m | 0.75-1.5 m/s | Branch fracture position; Main-branch fracture angle; Fracture inclination angle; Injection velocity |
| Zhou et al. (2024) | CFD-DEM coupling method | Rough single fracture | 0.3 m × 0.05 m × 0.001 m | 0.05-0.2 m/s | Proppant diameter; Injection velocity; Fractal dimension; Graded injection |
| Gong et al. (2024) | CFD-DEM coupling method | Single fracture | 0.14 m × 0.04 m × 0.005 m | 0.2 m/s | Proppant diameter; Cohesion energy density; The critical ratio of the fracture width to the mean proppant; Fluid leak-off |
| Zhang et al. (2025) | Novel hybrid CFD-DEM model | Complex fracture network | 0.05 m × 0.03 mm × 0.008 m | 0.1 m/s | Number of BFs; Roughness of BFs |
| Yang et al. (2025) | Eulerian-Eulerian method | Complex fracture network | 300 m × 50 m × 50 m | 0.15-0.35 $m^3$/min | Proppant diameter; Injection rate; Approach angle; Stress difference |
| Liu et al. (2025) | Eulerian-Eulerian method | Complex fracture network | 600 m × 400 m × 50 m | 0.05 $m^3$/s | Proppant diameter; Proppant type; Reservoir temperature |

microscopic transport mechanisms in non-planar fracture networks. Finally, based on the constructed model, the effects of different operational parameters (fracturing fluid viscosity and injection rate) and material parameters (proppant diameter and density) on the transport mechanisms and patterns within the fracture network are systematically investigated. The research findings can provide a theoretical reference for parameter optimization and process design in large-scale propped fracturing treatments of shale reservoirs.

## 2. Methodology

The Multiphase Particle-in-Cell (MP-PIC) method, originally pioneered by Andrews and O'Rourke, is an advanced numerical technique for simulating particle-fluid interactions (Andrews & O'Rourke, 1996; O'Rourke & Snider, 2010). It mathematically groups the discrete particle phase into computational "parcels" to efficiently resolve interphase interactions, as illustrated in Fig. 1. By combining strict physical conservation laws with high computational efficiency, the MP-PIC method is uniquely suited for simulating complex systems such as multiphase flows and dense particle transport phenomena (Mao et al., 2019; Patankar & Joseph, 2001; Tsai et al., 2013; Wang et al., 2026; Zeng et al., 2019). In this study, the proppant transport model is formulated within a hybrid Eulerian-Lagrangian multiphase flow framework, which simultaneously governs the fluid and particle phases. Specifically, the fluid phase is resolved as a continuous medium using the Eulerian approach, while the particle phase is explicitly tracked via a Lagrangian method. This fully coupled approach accurately captures both the macroscopic fluid hydrodynamics and the microscopic proppant

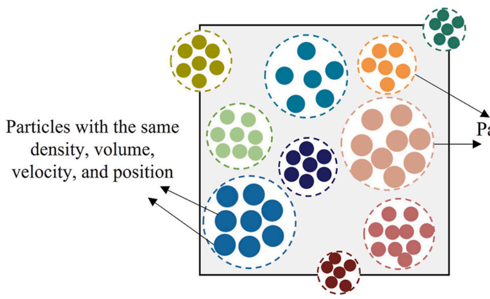


**Fig. 1.** Schematic diagram of the solution approach for Particle-in-Cell method with parcels.

transport dynamics within the complex fracture flow fields (Mao et al., 2021).

### 2.1. Model assumptions and boundary conditions

#### 2.1.1. Model assumptions

To effectively balance computational efficiency and simulation accuracy for large-scale complex fracture networks, the MP-PIC mathematical model established in this study is based on the following key assumptions.

(1) Fluid Phase: The fracturing fluid is assumed to be an incompressible Newtonian fluid, and temperature variations during the transport process are ignored.
(2) Particle Phase: Proppant particles are treated as rigid spheres. All particles within the same computational parcel share identical properties, including density, diameter, and velocity.
(3) Interphase Interactions: The deformation of proppant particles caused by compressive forces is neglected; only momentum exchange between particles and the stress distribution induced by collisions are considered.
(4) Fracture Geometry: The fracture walls are assumed to remain static during the fluid injection and proppant placement processes. The dynamic evolution of fracture width driven by fluid pressure is not considered, allowing this study to focus purely on the multiphase transport mechanisms of the proppant.

#### 2.1.2. Boundary conditions

To properly solve the MP-PIC governing equations, the boundary conditions for the computational domain are defined as follows.

(1) Inlet Boundary: A velocity inlet condition is applied. The initial velocity of the fluid phase is calculated and set based on the operational injection rate; simultaneously, the volume fraction of the proppant particles is specified at the inlet according to the proppant concentration.
(2) Outlet Boundary: A pressure outlet condition is applied. The outlet pressure is set to a constant reservoir ambient pressure to simulate the fluid flow into the deeper formation.
(3) Fluid Phase Wall Boundary: The non-planar fracture walls follow a no-slip boundary condition, meaning that the fluid velocity at the wall is zero.
(4) Particle Phase Wall Boundary: To accurately capture the interaction between proppants and rock walls in complex non-planar fractures, the fracture walls are set as reflection boundaries.

### 2.2. Continuum phase (fluid phase) governing equation

The fluid phase is governed by the continuity and momentum equations. Fluid flow follows the incompressible Navier-Stokes equations. The rate of fluid mass increase per unit time equals the net flux into the control volume. Due to fluid incompressibility, this simplifies to the conservation of volume fraction. The continuity equation for interphase mass transfer is as follows:

$$\frac{\partial(\alpha_f\rho_f)}{\partial t}+\nabla\cdot(\alpha_f\rho_f u_f)=0 \tag{1}$$

Where $f$ is the fluid phase symbol; $\alpha_f$ denotes the fluid volume fraction; $u_f$ represents the fluid velocity; and $\rho_f$ is the fluid density.

The momentum equation comprises the following terms: the inertial term (the local time derivative and convective term), the pressure gradient term, the fluid-particle momentum exchange term, the gravitational force term, and the fluid viscous stress term.

$$\frac{\partial(\alpha_f\rho_f u_f)}{\partial t}+\nabla\cdot(\alpha_f\rho_f u_f u_f)=-\nabla p-F_{fp}+\alpha_f\rho_f g+\nabla\cdot\alpha_f\tau_f \tag{2}$$

Where $p$ represents fluid pressure; $F_{fp}$ denotes the momentum change rate per unit volume between the fluid phase and particle phase; $g$ is the gravitational acceleration; $\mu_f$ represents fluid viscosity, and $\tau_f$ is the fluid stress tensor.

The equations for the non-hydrostatic component of the stress tensor and for a Newtonian fluid are as follows:

$$S=\frac{1}{2}\left(\nabla\boldsymbol{u}_f+(\nabla\boldsymbol{u}_f)^{\mathrm{T}}\right) \tag{3}$$

$$\tau_f=2\mu_f S-\frac{2}{3}\mu_f(\nabla\cdot\boldsymbol{u}_f)\mathbf{I} \tag{4}$$

### 2.3. Discrete phase (particle) governing equation

The dynamics of the particle system are characterized by the time evolution of a probability distribution function $f(x,u_p,\rho_p,V_p,t)$, which is governed by the generalized Boltzmann equation.

The conservation equation for the particle phase incorporates a convection term $(u_p\cdot\nabla_x f)$, an acceleration term $(a\cdot\nabla_{u_p}f)$, and collision term (representing changes in the distribution function induced by inter-particle collisions). The evolution of this probability distribution function is described by the following equation:

$$\frac{\partial f}{\partial t}+u_p\cdot\nabla_x f+a\cdot\nabla_{u_p}f=\left(\frac{\partial f}{\partial t}\right)_{\text{coll}}^{D} \tag{5}$$

Where $x$ represents particle position; $u_p$ is particle velocity; $\rho_p$ denotes particle density; $V_p$ is particle volume; $t$ is time; $a$ is the external force per unit mass acting on a particle (acceleration), the subscripts $x$ and $u_p$ represent gradient operators with respect to spatial and velocity coordinates, respectively, the subscript $p$ represents particle phase sign, and the $\left(\frac{\partial f}{\partial t}\right)_{\text{coll}}^{D}$ term denotes the net time rate of change induced by particle collisions (Andrews & O'Rourke, 1996; Williams, 2018).

During the solution process, the particle phase is modeled as discrete computational parcels. Each parcel comprises a group of particles sharing identical properties, including density, volume, velocity, and position. The trajectory of each parcel is tracked using Newton's second law of motion. The Lagrangian equation of motion for the particles accounts for the following forces: (1) the interphase drag force arising from the relative velocity between the particles and the fluid, (2) the fluid pressure gradient force, (3) gravity, (4) the inter-particle solid stress, and (5) collision damping.

$$a=\frac{du_p}{dt}=D_p(u_f-u_p)-\frac{1}{\rho_p}\nabla p+g-\frac{1}{\alpha_p\rho_p}\nabla\sigma_p+\frac{\langle u_p\rangle-u_p}{\tau_D} \tag{6}$$

Where $D_p$ denotes the drag coefficient; $u_p$ is particle velocity; $u_f$ represents the fluid velocity; $\tau_D$ is the relaxation time; $p$ is pressure; $\rho_p$ is particle density; $\alpha_p$ represents particle volume fraction; $\sigma_p = \frac{P_s \alpha_p^b}{\max(\alpha_{cp}-\alpha_p, \varepsilon(1-\alpha_p))}$ is particle normal stress, which simulates the physical processes of inter-particle collisions and elastic recovery to prevent excessive particle accumulation (Harris & Crighton, 1994). This stress represents derived from the Harris-Crighton model, where $P_s$ is the stress constant, $\alpha_{cp}$ denotes the packed particle volume fraction, and $b \in [2, 5]$ is a constant (Auzerais et al., 1988), $\varepsilon$ is used to avoid singularities within parcels (Snider, 2001), typically on the order of $10^{-7}$.

The above drag coefficient is calculated by the following equation (Wen & Yu, 1966):

$$D_p = C_d \frac{3}{8} \frac{\rho_f}{\rho_p} \frac{|u_f - u_p|}{r_p} \tag{7}$$

$$S_\alpha^s(s) = \begin{cases} 1 - s, s \in [0, 1), \text{corresponding to the left/bottom/back nodes}(\alpha = 0) \\ s, s \in [0, 1), \text{corresponding to the right/top/front nodes}(\alpha = 1) \\ 0, s \geq 1 \text{ or } s < 0, \text{exceeding the interpolation interval, the node is no longer contributing weight} \end{cases} \tag{12}$$

Where $C_d$ represents the dimensionless coefficient of interphase drag; Re denotes Reynolds number; $r_p$ is particle radius; and $V_p$ is particle volume, assuming spherical particles.

### 2.4. Solution and coupling schemes

In the MP-PIC method, fluid properties (e.g., pressure, velocity) are stored at regular Eulerian grid nodes, while particle positions typically remain at arbitrary Lagrangian points. To calculate the fluid forces (e.g., drag force) acting on particles, fluid properties must be interpolated to the particles' locations. Conversely, the particle volume fraction also needs to be interpolated back to the Eulerian grid nodes. This interpolation process is termed particle-grid interaction.

The fluid and particle phases are coupled through interphase momentum transfer, where the momentum exchange between the fluid and particles is implemented via volume integration:

$$F_{fp} = \iiint f V_p \rho_p \left[ D_p (u_f - u_p) - \frac{1}{\rho_p} \nabla p \right] dV_p d\rho_p du_p \tag{8}$$

The particle volume fraction model at the grid nodes, constructed using trilinear interpolation, grid mapping, normalized coordinates, and vertex weights, enables the precise transfer of discrete particle information to the continuous grid.

Considering a structured grid system in three-dimensional space, the grid cells are indexed by $(i, j, k) \in \mathbb{Z}^3$, and their spatial extent is defined as:

$$\Omega_{ijk} = [i\Delta x, (i+1)\Delta x] \times [j\Delta y, (j+1)\Delta y] \times [k\Delta z, (k+1)\Delta z] \tag{9}$$

Where $\Omega_{ijk}$ represents indexed as $(i, j, k)$ the grid cell; $\Delta x, \Delta y, \Delta z$ denotes the grid edge lengths, satisfying $\Delta x = x_{i+1} - x_i$, $\Delta y = y_{j+1} - y_j$, $\Delta z = z_{k+1} - z_k$.

The centroid position of a parcel is denoted as $x_p = (x_p, y_p, z_p)$, and the grid cell in which it resides is determined by coordinate projection:

$$(i, j, k) = \left( \frac{x_p}{\Delta x}, \frac{y_p}{\Delta y}, \frac{z_p}{\Delta z} \right) \tag{10}$$

To ensure that particles are fully contained within a single grid cell, the relative position of the particle within the grid cell (normalized coordinates) is defined as:

$$\xi = \frac{x_p - i\Delta x}{\Delta x}, \eta = \frac{y_p - j\Delta y}{\Delta y}, \zeta = \frac{z_p - k\Delta z}{\Delta z} \tag{11}$$

Where $\xi, \eta, \zeta \in [0, 1]$ denote the normalized coordinates. These coordinates normalize the physical space, describing the local position of the particle centroid relative to the grid cell vertices (e.g., $(\xi = 0, \eta = 0, \zeta = 0)$ corresponds to the bottom-left vertex of the grid cell, and $(\xi = 1, \eta = 1, \zeta = 1)$ corresponds to the top-right vertex). This provides a unified variable for subsequent interpolation and eliminating the influence of grid size on the interpolation formula.

The trilinear interpolation function is constructed as the product of one-dimensional linear along interpolations in three orthogonal directions, where the one-dimensional interpolation function is defined as:

Where $s \in \{\xi, \eta, \zeta\}$ is the interpolation function, represents the relative offset of the current position along the axis; $\alpha \in \{0, 1\}$ is the relative position of the neighboring node (e.g., $\alpha = 0$ corresponds to the $x = i\Delta x$, and $\alpha = 1$ corresponds to the $x = (i + 1)\Delta x$).

In three-dimensional space, the contribution of a grid cell vertex $(i + \alpha, j + \beta, k + \gamma)(\alpha, \beta, \gamma \in \{0, 1\})$ to the interpolation is determined by the product of the interpolation functions in the three orthogonal directions:

$$S_{ijk}^{\alpha\beta\gamma}(\xi, \eta, \zeta) = S_\xi^\alpha(\xi) \cdot S_\eta^\beta(\eta) \cdot S_\zeta^\gamma(\zeta) \tag{13}$$

Taking the volume fraction at the Eulerian grid nodes as an example for the derivation, the interpolation model for the particle volume fraction at thr grid nodes is expressed as follows:

Assuming the particle volume be $V_p$, its volume fraction $\phi_p$ is defined as the ratio of the particle volume to the grid cell volume. The volume fraction contribution of the particle to the target node $(i, j, k)$ is:

$$\Delta \alpha_{p,ijk} = \phi_p \cdot V_p \cdot S_{ijk}^{000}(\xi, \eta, \zeta) \tag{14}$$

Where $S_{ijk}^{000}(\xi, \eta, \zeta)$ represents the interpolation weight corresponding to the grid cell vertex where the particle centroid resides (When the particle is completely located at a vertex within the grid cell, i.e., $\xi = 0, \eta = 0, \zeta = 0$, the weight is determined by the normalized coordinates).

For a system containing $N_p$ particles, the final volume fraction at node $(i, j, k)$ is obtained by summing the contributions of all particles and applying normalization (Patankar & Joseph, 2001; Snider, 2001):

$$\alpha_{p,ijk} = \frac{1}{V_{ijk}} \sum_{p=1}^{N_p} \Delta \alpha_{p,ijk} \tag{15}$$

Where $V_{ijk} = \Delta x \Delta y \Delta z$ denotes the volume of the grid cell.

The core computational workflow and two-way coupling strategy of the MP-PIC model in this study are illustrated in Fig. 2. This cyclic iteration process primarily involves several key steps: First, parameters for the fluid phase, proppant parcels, and the initial computational mesh are initialized. Once initialization is complete, the Navier-Stokes equations are solved on the Eulerian mesh to determine the motion state of the background fluid phase. Subsequently, the process proceeds to the fluid-to-solid coupling stage: fluid velocity and pressure at the Eulerian mesh nodes are mapped to the locations of each parcel via interpolation, enabling the calculation of fluid drag, pressure gradient, and gravitational forces acting on the particles. After obtaining the forces, the

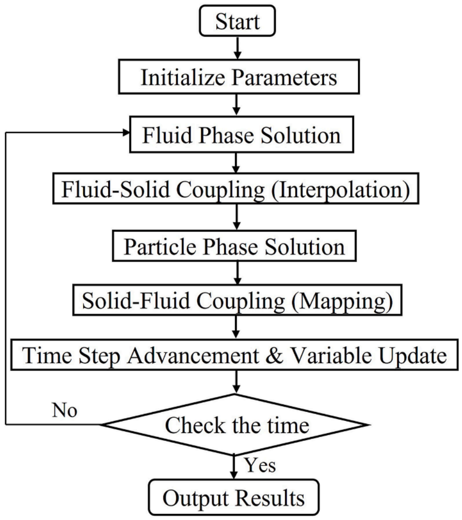


**Fig. 2.** Calculation flow chart.

Lagrangian method is employed to track parcel trajectories and calculate particle-particle collisions, completing the solution for the particle phase. Thereafter, the process enters the solid-to-fluid coupling stage: the volume fraction of the displaced parcels and their momentum exchange with the fluid are mapped back to the Eulerian grid nodes. Finally, the system updates the physical quantities for the next time step. The program continuously iterates through this two-way coupling process until the predefined total computational time steps are reached, at which point the simulation results are output.

## 3. Model validation

### 3.1. Experimental verification

To validate the accuracy of the proposed model, the numerical simulation results from this study are compared with the laboratory experimental results of Tong and Mohanty (2016). In the referenced experiment, an intersecting physical model comprising a main fracture and secondary fractures is constructed using transparent plexiglass plates. A screw pump equipped with a variable frequency drive (VFD) is utilized to inject the slurry at a constant rate from one end of the model, while a constant pressure boundary condition is applied at the outlet. During the experiment, a high-speed camera is employed to record the dynamic distribution patterns of the proppant at the complex intersection. In this study, a numerical model with the exact same dimensions as the experimental setup is constructed. Specifically: a main fracture length of 0.381 m, a height of 0.762 m, and a width of 0.002 m, with a secondary fracture length of 0.1905 m, and all other parameters consistent with those of the main fracture. The properties of the proppant and fluid are provided in Table 2. The slurry is injected into the model from the right side at a flow velocity of 0.1 m/s. The proppant distribution after 20 s and 40 s of injection is then compared with the experimental observations to assess the model's accuracy.

**Table 2**
Model validation data table.

| Parameters | Value |
|---|---|
| Proppant diameter | 0.6 mm |
| Inlet proppant concentration | 0.02 |
| Proppant density | 2650 kg/m$^3$ |
| Fluid density | 1000 kg/m$^3$ |
| Fluid viscosity | 1 mPa s |
| Injection velocity | 0.1 m/s |
| Injection time | 20/40 s |
| Outlet pressure | 0.1 MPa |

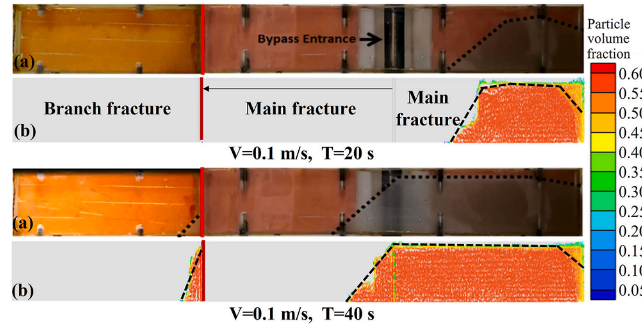


**Fig. 3.** Comparison of the proppant distribution with experimental results from Tong and Mohanty (2016), at inlet velocity of the proppant is 0.1 m/s. The time of 20 and 40 s. (a) Experimental results of Tong and Mohanty (b) Numerical results of our model.

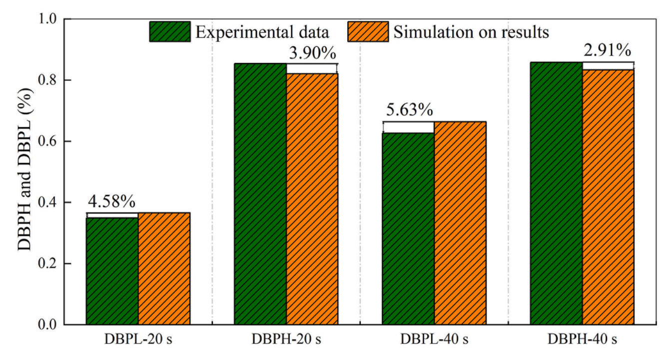


**Fig. 4.** DPBH and DPBL comparison of Tong and Mohant's experimental results and our model results.

The simulation results demonstrate that, at the same injection velocity, the proppant moves farther towards the far end of the fracture as the injection time increases. The sand bed height in the secondary fracture increases, and at the junction with the main fracture, a sudden drop forms due to flow diversion, creating an inflection point. The experimental results closely match the proppant distribution simulated by the model (Fig. 3). A comparison of the dimensionless proppant sand bed height (DPBH, defined as the ratio of the proppant sand bed height to the fracture height) and length (DPBL, defined as the ratio of the proppant transport length to the main fracture length) at different injection times yields relative errors of 4.58%, 3.90%, 5.63%, and 2.91%, respectively (Fig. 4). These results validate the accuracy of the proposed model, confirming its reliability for studying proppant transport in complex fracture networks. The primary sources of error are attributed to differences in injection methods and the roughness of the fracture walls during the physical experiments.

### 3.2. Grid independence verification

To preclude the influence of mesh size on the numerical simulation results, a mesh independence test is performed in this section. Two mesh configurations physical models are developed for comparative calculation: a base mesh (0.1 m × 0.1 m) and a refined mesh (0.05 m × 0.05 m). As illustrated in Fig. 5, the simulation results indicate that the proppant transport trends and distribution patterns are fundamentally consistent across both mesh sizes. This suggests that the computational results have converged at the current mesh scale, demonstrating robust mesh independence. To effectively balance balancing solution accuracy and computational efficiency, the 0.1 m × 0.1 m mesh scheme is selected for subsequent research.

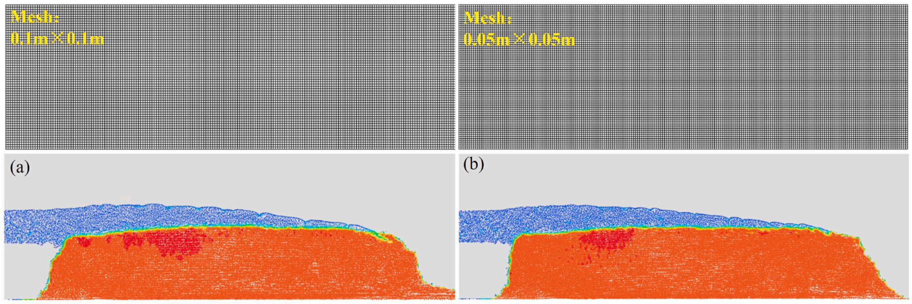


**Fig. 5.** Simulation results under different grid sizes.

## 4. Results and discussion

### 4.1. Physical model construction and parameter input

Given the high brittleness of shale reservoirs and the extensive development of natural weak planes (e.g., fractures and bedding planes), the intertwining of tensile and shear failures during hydraulic fracturing readily leads to the formation of complex fracture networks. Drawing on the research of Yu et al. (2019), a field-scale physical model with dimensions of 50 m × 50 m × 5 m is constructed. The core of the modeling process lies in the precise extraction of geometric features and the spatial mesh discretization: first, the geometric morphology of the actual outcrop fracture network is extracted proportionally and imported into the numerical model; subsequently, a high-quality hexahedral mesh is employed for the discretization of the smooth-wall model. To balance computational efficiency and numerical precision, the mesh size is set to 0.1 m × 0.1 m, resulting in a total of approximately 2,214,133 grid cells. The fracture network is primarily composed of two components: (1) Main fractures: Primary fractures formed during hydraulic fracturing, initiated by high-pressure fluid injection; (2) Secondary fractures: This category encompasses all branch fractures developed alongside the main fractures, as well as natural weak planes activated during hydraulic fracture propagation (Fig. 6). The x-direction represents the minimum principal stress, and the y-direction represents the maximum principal stress. Field data indicate that shear fractures (secondary fractures) are narrower than tensile fractures. In this model, secondary fractures have a width of 3 mm, while main fractures have a width of 6 mm. Additional input parameters are listed in Table 3. The inlet is a constant current injection, and the outlet boundary is open. The study examines the effects of proppant density, diameter, fluid viscosity, and injection rate on proppant transport and placement.

**Table 3**
Basic parameter inputs of the fracture network model based on outcrop.

| Parameters | Value |
|---|---|
| Hydraulic fracture width | 6 mm |
| Fracture height | 5 m |
| Bedding fracture; Secondary fracture width | 3 mm |
| Injection rate | 2 $m^3$/min |
| Fluid viscosity | 1 mPa s |
| Proppant diameter | 0.4 mm |
| Proppant density | 2400 kg/$m^3$ |
| Fluid density | 1000 kg/$m^3$ |
| Injection time | 450 s |

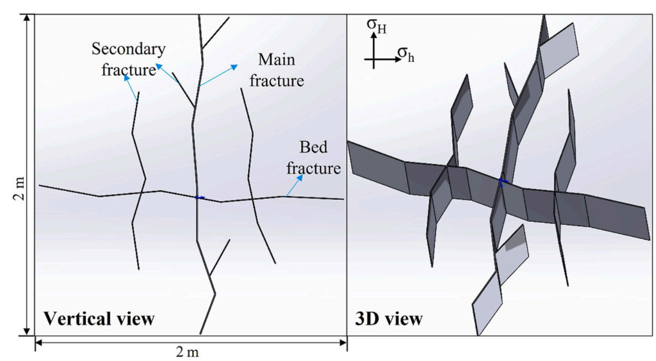


**Fig. 7.** Schematic of the local small-scale physical model constructed based on the model in Fig. 4.

### 4.2. Transport mechanism of proppants in fracture networks

To further investigate proppant transport within non-planar fractures, a small-scale localized fracture network model (2 m × 2 m) is extracted from the previously established model (Fig. 6). The physical model (Fig. 7) is constructed with consistent parameter settings, and the total simulation time is set to 30 s. Using this localized fracture geometry model, the transport and placement mechanisms of proppants in both main and secondary fractures are systematically studied. The simulation results are presented in Figs. 8 and 9.

An analysis of proppant transport within the fracture network reveals that the distribution is highly uneven due to the curved geometry of the fractures. In regions with larger deflection angles, local proppant

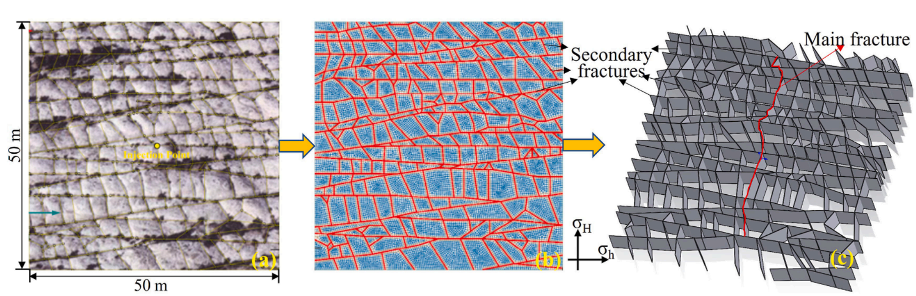


**Fig. 6.** Schematic diagram of the fracture network physical model established based on an authentic outcrop: (a) Authentic core outcrop; (b) Model characterized after image processing; (c) Fracture network physical model proposed in this study.

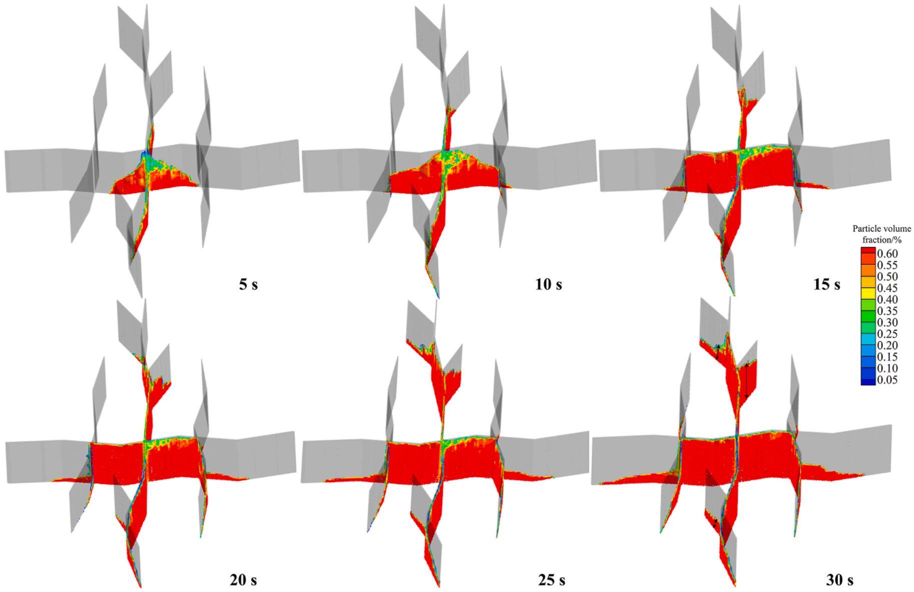


**Fig. 8.** Cloud map of proppant transport in a complex fracture network at different times.

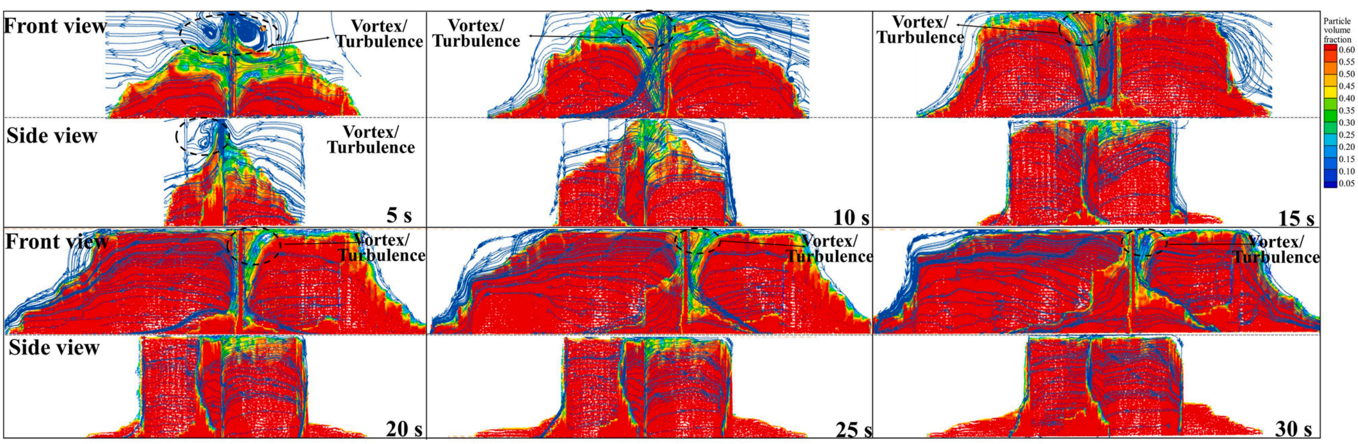


**Fig. 9.** Streamline diagrams of proppant transport in a complex fracture network at different times (front view/side view).

concentration increases, leading to intensified particle collisions and rapid settling due to kinetic energy dissipation. Simultaneously, the curved sections of the fractures tend to induce turbulence and vortices, which re-entrain proppants and transport them toward the fracture toe or into secondary fractures. This alternating process results in an undulating sand bed surface in the main fracture. At junctions with secondary fractures, flow diversion causes a sudden drop in proppant concentration, creating a distinct inflection point. Proppants either continue along the main fracture, are diverted into secondary fractures, or settle due to gravity. The closer a secondary fracture is to the injection point, the more proppant it receives. Additionally, a larger intersection angle between the secondary and main fractures leads to increased diversion resistance, which reduces the fluid velocity and proppant transport capacity. Consequently, less proppant enters these secondary fractures, resulting in a lower sand bed height. Because the fluid velocity in the secondary fractures is relatively low, there is no significant dune fluidization, and the sand bed exhibits a gentle downward slope (Fig. 8, $t = 30$ s). Throughout the network, proppant transport is influenced by highly continuous bedding planes and secondary fractures, forming distinct dominant flow channels along the x- and y-directions (i.e., the main fracture and near-wellbore secondary fractures, respectively). In the main fracture, proppants propagate longitudinally into perpendicular secondary fractures, while in the near-wellbore secondary fractures, they propagate laterally into parallel secondary fractures. Overall, proppants migrate propagates from these preferential channels to surrounding fracture regions.

To further elucidate the underlying transport mechanisms within the complex fracture network, the dynamic evolution of proppant placement is analyzed across three distinct injection stages: In the initial stage, the injection of high-velocity slurry into fractures with narrow entry points, abrupt changes in fracture width, and intersections with natural fractures triggers shear flow separation. The high Reynolds number of the fluid leads to the dominance of inertial forces, forming large-scale vortices (Fig. 9, $t = 5$ s, 10s). Proppant particles are carried into these vortices at high velocity, following irregular motion trajectories that result in extreme spatial heterogeneity both vertically (fracture height) and horizontally (fracture length). High sand beds form in regions with intense vortex activity, while low or sand-free zones develop in vortex cores or energy dissipation regions. This vortex phenomenon is especially pronounced in the near-wellbore zone, where the flow follows a circular pattern, resulting in a low proppant concentration in the center and higher concentrations in the upper and lower regions (Fig. 9, $t = 5$ s, 10 s).

During the mid-injection stage, as the sand bed height increases, the narrowing gap between the fracture top and the proppant bed apex reduces the flow channel's cross-sectional area. This accelerates both the fracturing fluid and the proppants, leading to the fluidization of the uppermost proppant layer. Erosion at the periphery re-entrains the proppants into the flow, pushing them deeper into the fracture. However, due to energy dissipation, the proppants quickly resettle, creating a cyclic process of re-entrainment and resettlement. This results in an upward-sloping sand bed distribution (Fig. 9, $t = 10$ s, 15 s). At this stage, vortex streamlines primarily curve upward in a crescent shape. While these vortices are less intense than during the initial phase, they still contribute to non-uniform proppant distribution. The vortex zone propagates toward the fracture tip, and as vortices migrate over long distances, fluid loss reduces the flow velocity. With higher proppant concentrations, fluid viscosity increases, causing large vortices to fragment. The smaller vortices, driven by particle wakes, trigger proppant settling (Fig. 9, $t = 20$ s).

In the late injection stage, a significant amount of proppant accumulates in the near-wellbore zone. As the fracturing fluid moves toward the fracture tip, the Reynolds number decreases, shifting the flow regime from turbulent to laminar flow due to the dominance of viscous forces. This results in reduced flow velocity and turbulence intensity, with large vortices dissipating and smaller vortices gradually vanishing due to viscous dissipation (Fig. 9, $t = 25$ s, 30 s). Proppant settling accelerates under gravity, becoming the dominant process, which leads to a downward slope in the sand bed (Fig. 9). In secondary fractures, vortices are weaker due to lower flow velocity, reducing the sand-carrying capacity. Unlike that in the main fracture, the sand bed in secondary fractures has a smaller height and a gentle downward slope.

### 4.3. *Effect of proppant density on proppant transport in fracture networks*

The proppant planar sweep efficiency and distribution uniformity within the fracture network directly influence reservoir stimulation effectiveness. To evaluate this, two quantitative parameters are proposed in this study:

First, the proppant planar sweep coefficient ($E_A$), defined as the ratio of the proppant's longitudinal and transverse sweep area ($S_{sweep}$) within the fracture network to the total projected area ($S_{total}$) of the model (viewed from the top perspective). This coefficient characterizes the proppant's coverage capability in the plane, with a larger ratio indicating a broader sweep range of the proppant.

$$E_A = \frac{S_{sweep}}{S_{total}} \tag{16}$$

Second, the proppant planar sweep uniformity coefficient ($C_U$), defined as the ratio of the minimum distance ($L_{min}$) from the center of gravity to the boundary within the swept range to the maximum distance ($L_{max}$). This coefficient is used to assess the distribution uniformity of the proppant in the plane, with a larger ratio indicating a more uniform distribution of the proppant across the plane.

$$C_U = \frac{L_{min}}{L_{max}} \tag{17}$$

Based on the physical model established in Fig. 6 and the input parameters detailed in Table 1, this study simulates proppant transport dynamics within complex fracture networks under varying proppant densities (2000, 2200, 2400, and 2600 kg/m$^3$). The total simulated injection time is set to 450 s, and the corresponding results are presented in Fig. 10.

The simulation results indicate that proppant density significantly influences the transport behavior in both the main fracture and the secondary fractures (which encompass highly continuous bedding planes and branch fractures). In the presence of multiple highly continuous secondary fractures, dominant transport channels predominantly develop in the near-wellbore region. Conversely, in the distal regions, deep proppant transport within the secondary fractures progressively diminishes; proppants partially accumulate at the fracture mouths, forming relatively low sand dunes, and the height of the proppant bed shows a stepwise declining trend as the number of secondary fractures increases. Due to the flow diversion effect of the secondary fractures, the fluid velocity in the main fracture decreases progressively. Coupled with the larger fracture width, this facilitates proppants settling, resulting in an overall higher sand dune within the main fracture.

Notably, the proppant distribution within the main fracture shows no significant difference across varying proppant densities. However, the proppant distribution within the near-wellbore secondary fractures varies considerably with density. At low densities (e.g., 2000 kg/m$^3$), proppants are less prone to settling, the accelerated flow velocity at the mouths of the secondary fractures readily generates vortices, promoting proppant transport toward the fracture tops and distal ends (Fig. 10a and b). This extends the dominant transport channels further along the x-direction into the secondary fractures, resulting in a larger, and more uniform planar sweep area (with a density of 2000 kg/m$^3$, the planar sweep coefficient is 0.1456, and the uniformity coefficient is 0.2941, Fig. 11). As the density increases, gravity dominates and the suspension capacity diminishes, causing proppants to rapidly settle at the bottom near the fracture mouth. However, as the dune height increases, the restricted cross-sectional area forces the local fluid velocity to rise, which re-entrains the proppants and transports them deeper along the dominant channels. Consequently, the sand bed height in the fracture initially presents a gentle upward slope, followed by a gradual decline as the velocity eventually dissipates (Fig. 10c and d). In the distal main

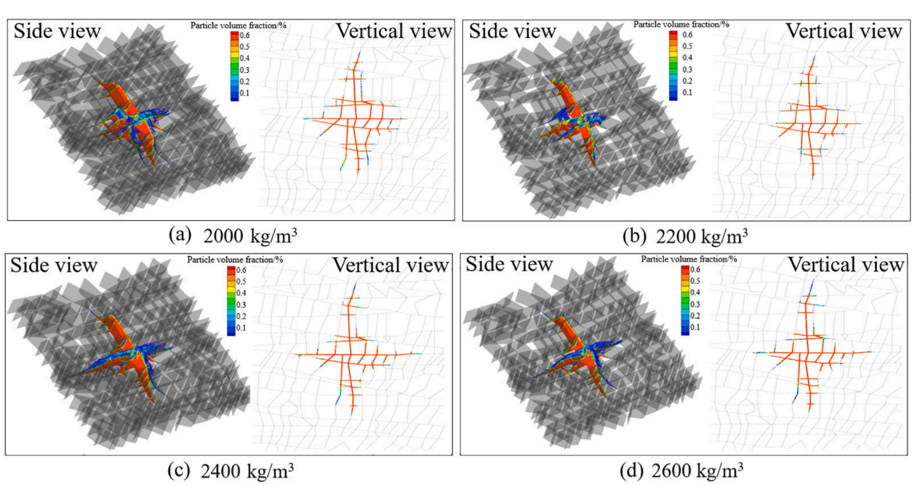


**Fig. 10.** Simulation results of proppant transport in the fracture network under different proppant densities.

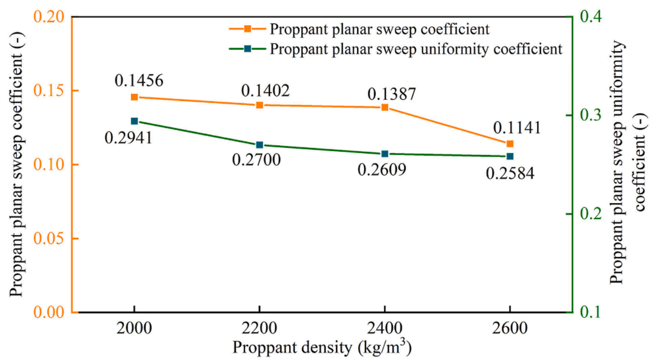


**Fig. 11.** Variation of proppant planar sweep coefficient and proppant planar sweep uniformity coefficient under different proppant densities.

fracture, the fluid velocity is inherently low, and the diversion velocity into secondary fractures is even lower. Therefore, the deep-transport phenomena observed near the wellbore do not occur here; instead, high-density proppants primarily accumulate at the fracture mouths, causing a "plugging" effect. Along the dominant transport channels, the farther the distance the injection point, the less proppant enters the flanking secondary fractures, leading to a smaller sweep area and stronger heterogeneity (at 2600 kg/m$^3$, the planar sweep coefficient drops to 0.1141, and the sweep uniformity coefficient is 0.2584, Fig. 11). The overall distribution assumes a cross-shaped pattern, which becomes increasingly pronounced at higher proppant densities (Fig. 10).

A comparison of the planar proppant sweep coefficient and the uniformity coefficient reveals that as the proppant density increases from 2000 to 2600 kg/m$^3$, both the sweep area and placement uniformity within the fracture network exhibit a stepwise decline. Specifically, when the density increases from 2000 to 2400 kg/m$^3$, the planar sweep coefficient experiences only a marginal decrease from 0.1456 to 0.1387 (a reduction of 4.7%), indicating that the influence of density on the sweep area is relatively weak within this range. However, as the proppant density further increases to 2600 kg/m$^3$, the planar sweep coefficient drops sharply to 0.1141, a substantial reduction of 17.7% compared to the 2400 kg/m$^3$ case, and the sweep uniformity coefficient correspondingly decreases from 0.2941 to 0.2584. These quantitative results demonstrate that a critical threshold exists for the impact of increasing proppant density on the planar sweep area; once this threshold is exceeded, higher densities severely restrict the effective proppant placement and mechanical support within the fracture network (Fig. 11).

In summary, it is highly recommended that field operations adopt a staged proppant injection strategy. Initially, low-density proppants should be injected to effectively fill the secondary fractures. Subsequently, high-density proppants should be pumped to transport along the dominant flow channels toward the fracture distal ends. Furthermore, fully filling the fracture mouths with proppant can effectively maximize the overall conductivity of the hydraulic fracture system.

### *4.4. Effect of proppant diameter on proppant transport in fracture networks*

Based on the physical model established in Fig. 6 and the input parameters detailed in Table 1, this study simulates proppant transport in complex fracture networks with varying proppant diameters (0.2, 0.4, 0.6, and 0.8 mm). The injection time is 450 s, with results shown in Fig. 12.

The simulation results indicate that the effect of proppant diameter on placement patterns in the fracture network is similar to that of proppant density. For smaller proppant sizes, the sand dune height within the main fracture remains relatively low, yet its surface profile exhibits more pronounced fluctuations. This is primarily because smaller particles are more easily entrained, forming a thicker suspension layer. Consequently, a substantial amount of proppant is diverted into the secondary fractures, resulting in a relatively uniform sweep, although the deep transport distance along the dominant channels is somewhat restricted. With diameters of 0.6 and 0.8 mm, the planar sweep coefficients are 0.1585 and 0.1439, with uniformity coefficients of 0.3938 and 0.2737, respectively, (Fig. 12). Smaller diameters also lead to higher proppant concentrations at the fracture top and greater sand bed heights in the distal region. This suggests that smaller proppants are highly conducive to propping secondary fractures. Conversely, as the proppant diameter increases, flow velocity along the preferential transport channel rises due to a reduced fluid flow path, causing proppants to be entrained further into the distal region. However, due to their larger mass, the suspension capacity diminishes, and vortex effects become negligible, leading to a lower accumulation of proppants at the fracture's distal end and a flatter bed surface near the wellbore. Furthermore, because the secondary fractures are relatively narrow, large proppants attempting to enter these branches are highly susceptible to bridging and plugging. Consequently, the sweep range becomes more non-uniform; at 1.0 and 1.2 mm, the planar sweep coefficients drop to 0.1331 and 0.1237, with uniformity coefficients of 0.2655 and 0.2599, respectively, (Fig. 13).

A comparative analysis reveals that as the proppant diameter increases, the sweep pattern becomes more distinctly cross-shaped, with

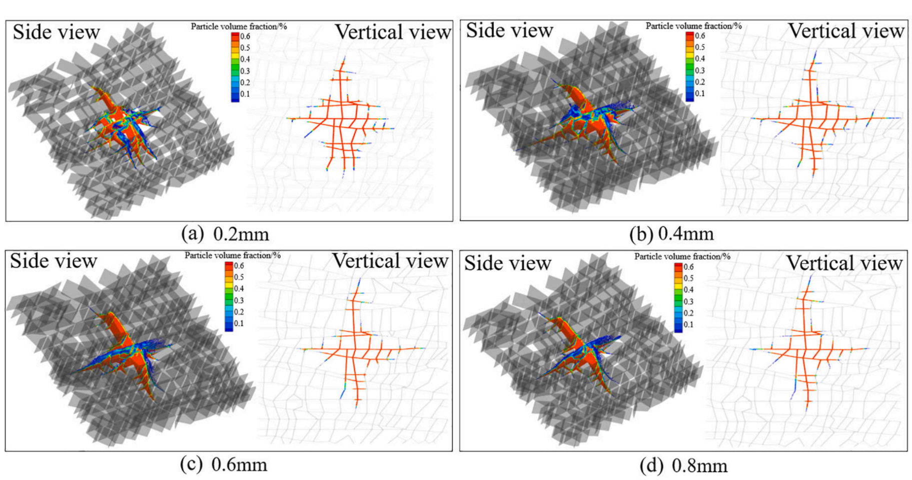


**Fig. 12.** Simulation results of proppant transport in the fracture network under different proppant diameters.

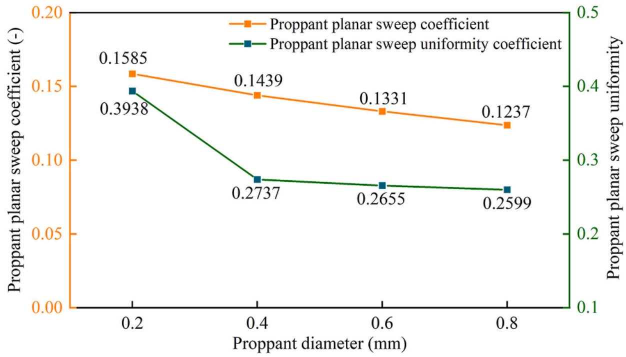


**Fig. 13.** Variation of proppant planar sweep coefficient and proppant planar sweep uniformity coefficient under different proppant diameters.

increasing non-uniformity. The planar sweep coefficient exhibits a nearly linear decline from 0.1585 (at 0.6 mm) to 0.1237 (at 1.2 mm). The uniformity coefficient for 0.8 mm drops by 34% compared to 0.6 mm, while only a 5% reduction occurs at 1.2 mm relative to 0.8 mm. These results demonstrate that proppant diameter has a critical threshold effect on sweep uniformity: once this threshold is exceeded, further increases in diameter have minimal effect on the uniformity of proppant distribution within the fracture network (Fig. 13).

Synthesizing these findings, it is evident that employing exclusively undersized or oversized proppants is detrimental to effective fracture packing. Extremely small particles resist settling and are highly susceptible to being flushed out by the fracturing fluid during flowback, leaving the hydraulic fractures inadequately supported. Conversely, excessively large particles induce severe distribution heterogeneity. Furthermore, the larger inter-particle void spaces can lead to uneven stress concentrations, causing proppant crushing and subsequent fracture plugging, which ultimately fails to establish effective oil and gas flow channels.

Therefore, field operations should adopt a multi-stage injection strategy. Small-diameter proppants should be pumped first to deeply penetrate the secondary fractures and the distal regions of the main fracture, thereby maximizing the propped coverage area across the network. Subsequently, large-diameter proppants should be injected to pack the near-wellbore region, widening the propped aperture at the mouths of both the main and secondary fractures. This staged approach comprehensively enhances the overall effective conductivity of the fracture network.

### *4.5. Effect of fluid viscosity on proppant transport in fracture networks*

Building upon the physical model established in Fig. 6 and the input parameters detailed in Table 1, numerical simulations are conducted to investigate proppant transport dynamics within complex fracture networks under varying fracturing fluid viscosities (3, 10, 20, and 30 mPa s). The total simulated injection time is set to 450 s, and the corresponding results are illustrated in Fig. 14.

The simulation results show that the proppant sweep area varies significantly with fracturing fluid viscosity. At lower viscosities, both the lateral and longitudinal sweep extents are restricted, resulting in higher sand dunes overall (Fig. 14a and b). As the fluid viscosity increases, the fundamental flow regime undergoes a critical shift: the reduced Reynolds number directly suppresses turbulence, while the elevated fluid drag force markedly enhances the sand-carrying capacity. This mechanism thickens the suspension layer and diminishes the vortex-induced effects prevalent at lower viscosities. Driven by these mechanics, proppants are transported over greater distances and achieve a more uniform vertical distribution the within the fractures. The volume of proppants reaching deeper dominant channels and flanking lateral secondary fractures increases significantly, promoting their sequential diffusion across the fracture network. Consequently, high-viscosity fluids yield a considerably larger and more uniformly distributed sweep area (Fig. 14c and d).

A comparative analysis reveals that as the viscosity increases from 3 to 30 mPa s, both the proppant planar sweep area and the degree of uniformity exhibit a nearly linear growth trend. Specifically, the data indicate that the planar sweep coefficient increases significantly from 0.163 at a low viscosity (3 mPa s) to 0.2576 at a high viscosity (30 mPa s), representing a substantial increase of 58.0%. Correspondingly, the planar sweep uniformity coefficient also grows steadily from 0.4072 to 0.4537 (an increase of 11.4%). These results demonstrate that elevating the fracturing fluid viscosity significantly enhances the overall proppant placement performance (Fig. 15).

Comprehensive analysis suggests that moderate increases in fluid viscosity significantly improve proppant transport into deeper regions of both main and secondary fractures, thereby maximizing the proppant coverage area and promoting uniform distribution. However, employing excessively high viscosity fluids not only risks severe formation damage but also hinders the vertical settling of high-concentration proppants. This ultimately compromises the effective mechanical support of the overall fracture geometry.

### *4.6. Effect of injection rate on proppant transport in fracture networks*

Based on the physical model established in Fig. 6 and the input parameters detailed in Table 1, this study examines proppant transport dynamics within complex fracture networks under varying injection rates (1, 2, 3, and 4 $m^3$/min). With a constant injected fluid volume, the corresponding injection durations are 900, 450, 300, and 225 s, respectively, and the corresponding results are presented in Fig. 16.

The simulation results demonstrate that the injection rate plays a critical role in proppant transport within complex fractures. At lower injection rates (e.g., 1 $m^3$/min), proppants predominantly propagate uniformly along the dominant flow channels. However, due to the low flow velocity and the substantial increase in energy dissipation caused by flow diversion into secondary fractures, proppants exhibit limited capacity to reach the distal ends of both the main and secondary fractures. Consequently, the sand dune remains relatively high, exhibiting a gradual downward slope from the injection point toward the deeper regions (Fig. 16a and b). Under these conditions, the proppant sweep area is restricted but highly uniform (at 1 $m^3$/min, the planar sweep coefficient is 0.1438, and the uniformity coefficient is 0.4965, Fig. 17).

As the injection rate increases, the constricted effective flow path further accelerates the local fluid velocity, leading to an elevated fluid shear rate. Governed by the shear-thinning behavior of the fluid and Stokes' settling principles, the apparent viscosity decreases, which triggers vortex-induced flows within the secondary fractures. This mechanism suspends a noticeable concentration of proppant toward the fracture roof along the dominant flow channels. However, the scouring effect at higher velocities prevents complete blockage in the deep regions of the fractures. Instead, proppants are transported to the far end, while inflow into secondary fractures on both sides decreases, leading to a reduction in the overall sand dune height within secondary fractures. The sand dune profile exhibits a characteristic gentle upward slope near the wellbore and a gentle downward slope distally (Fig. 16b), resulting in increased non-uniformity in proppant distribution (at an injection rate of 2 $m^3$/min, the planar sweep coefficient increases to 0.1473, and the uniformity coefficient drops to 0.3603, Fig. 17).

With further increases in the injection rate, the proppant transport distances along the dominant channels also expand even further. Unlike the low-velocity case, the sand dune profile within the secondary fractures now shows a gradual downhill trend from the fracture mouth to the distal end (excepting the vortex effect at the fracture mouth). This shift occurs because the higher fluid velocities allow the proppants to retain sufficient momentum to resist settling and plugging as they advance distally. While they travel farther along the dominant fractures, the

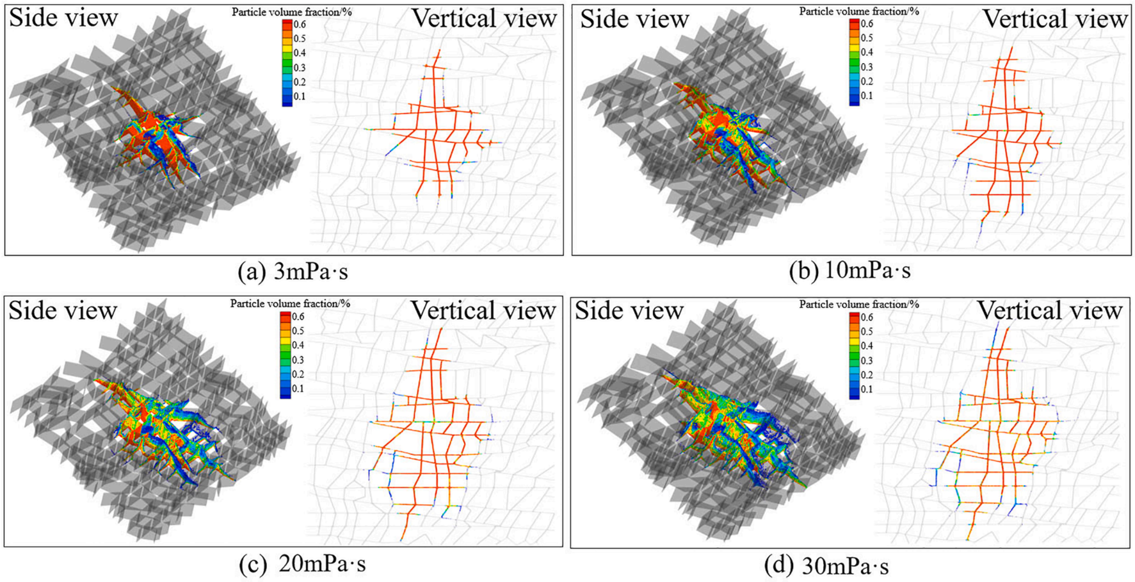


**Fig. 14.** Simulation results of proppant transport in the fracture network under different fluid viscosities.

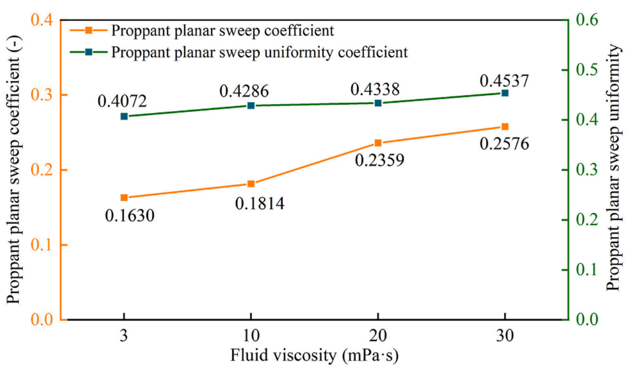


**Fig. 15.** Variation of proppant planar sweep coefficient and proppant planar sweep uniformity coefficient under different fluid viscosities.

overall sand dune height, the propped volume within the secondary fractures, and the comprehensive fracture propping effectiveness deteriorate significantly. Concurrently, due to the high overall network velocity, the transport behavior in the main fracture begins to resemble

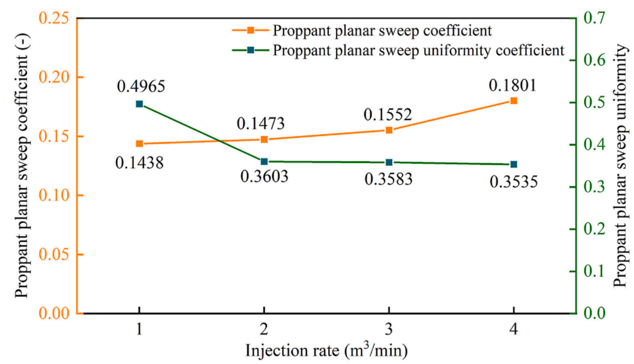


**Fig. 17.** Variation of proppant planar sweep coefficient and proppant planar sweep uniformity coefficient under different injection velocities.

that in the secondary fractures at lower velocities, the sand dune height drops, and the profile forms a gentle upward slope near the wellbore and a downward slope at the distal end. Additionally, the intense vortex effect at the fracture mouth pushes the entire dune body backward, severely compromising the propping effectiveness at the mouths of both

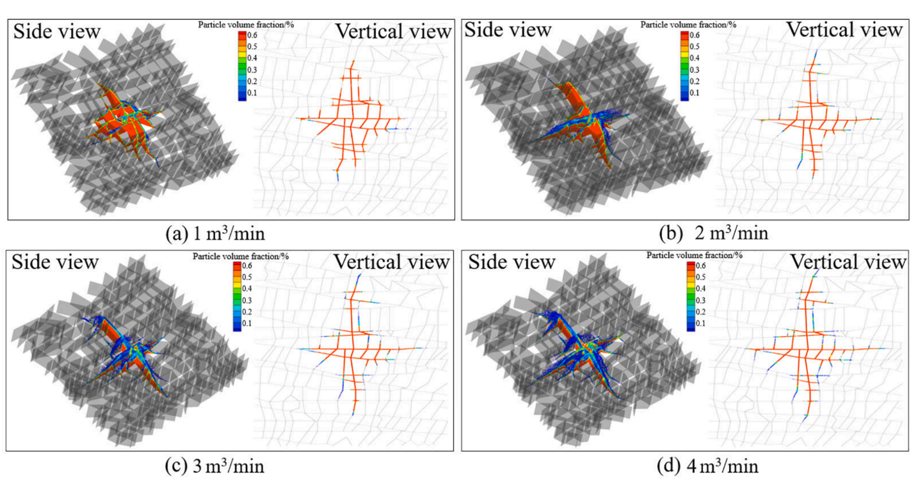


**Fig. 16.** Simulation results of proppant transport in the fracture network under different injection rates.

the main and secondary fractures. This occurs later than in secondary fractures due to variations in fracture width (Fig. 16c and d; Fig. 17).

Comparative analysis shows that the planar sweep coefficient of proppants increases with rising injection rate. Specifically, at the injection rate of 4 $m^3$/min, the planar sweep coefficient improves by 25.25% compared to 3 $m^3$/min, while the planar uniformity coefficient exhibits a fluctuating downward trend (Fig. 17).

Comprehensive analysis indicates that at low injection rates, complex fracture networks fail to achieve an effective propped volume. A moderate increase in injection rate enhances proppant transport within these fractures. However, excessively high flow velocities can trigger a near-wellbore scouring or necking effect, which hinders the formation of high-conductivity propped fractures. To address this, a staged pumping strategy of "high-rate transport followed by low-rate deposition" is highly recommended for field operations. This strategy starts with high-displacement transport to push proppants to the fracture tip, followed by reduced displacement to promote proppant deposition near the fracture mouth. This results in an ideal wedge-shaped proppant distribution, with the propped fracture width increasing from the distal end toward the fracture mouth, optimizing the propping effect.

## 5. Conclusions

This study develops a field-scale model for proppant transport within complex fracture networks using the Multiphase Particle-in-Cell (MP-PIC) method. The model is utilized to elucidate proppant transport mechanisms within curved fracture networks and comprehensively assess the impact of various factors on placement behaviors. The key findings are summarized as follows.

(1) Proppant distribution within the complex fracture network is highly heterogeneous, characterized by significant fluctuations in the sand dune height. The overall transport process is primarily influenced by secondary fractures, leading to the formation of two dominant flow channels: one propagating longitudinally along the main fracture and the other extending laterally along highly continuous secondary fractures in the near-wellbore region.

(2) The proppant transport process within the fracture network is characterized by a gradual migration from dominant flow channels to lateral secondary fractures. As the distance from the injection point increases, the proppant transport distance within the secondary fractures on both sides decreases. Additionally, the greater the angle between the secondary fractures and the main fracture, the smaller the volume of proppant that enters the secondary fractures.

(3) The sand dune profile within the fracture network is fundamentally governed by shifts in the fluid flow regime, transitioning among turbulent, transitional, and laminar states. Intense vortex formation predominantly occurs at the fracture mouths, exacerbating the longitudinal heterogeneity of the proppant distribution. As the fluid advances distally, these vortex effects dissipate, allowing gravity-driven deposition to dominate and resulting in a gradual decline in the dune height. While vortices can facilitate deeper proppant transport, their scouring effect concurrently reduces the dune height at the fracture mouths, thereby compromising the effective mechanical support at these critical junctions.

(4) Lower proppant densities and diameters reduce the likelihood of proppant settling, facilitating long-distance transport toward the distal fracture region. Conversely, high-density and large-diameter proppants settle rapidly and are highly susceptible to "bridging and plugging" at the fracture mouths, which restricts the sweep area and increases placement heterogeneity. Elevating the fracturing fluid viscosity markedly enhances the suspension capacity, promoting distal transport, expanding the planar sweep area, and improving overall uniformity. Similarly, higher injection rates propel proppants deeper into the main and secondary fractures, further broadening the sweep area; however, excessively high velocities intensify vortex phenomena, ultimately reducing the overall dune height and exacerbating distribution heterogeneity.

(5) For field fracturing design, a comprehensive staged pumping strategy, integrating variable injection rates, multi-stage proppant sizes/densities, and moderately elevated fluid viscosities, is highly recommended. During the early-to-mid stages of injection, a combination of high displacement, moderate-viscosity fluid, and small-diameter/low-density proppants should be employed. Leveraging the robust suspension capacity of this high-velocity, viscous fluid overcomes the settling resistance of small particles, effectively driving them deep into the secondary fractures and maximizing the planar propped sweep area. In the mid-to-late stages, the strategy should pivot to low displacement coupled with large-diameter/high-density proppants. This leverages the rapid settling mechanics of larger, heavier particles under low flow rates to establish high-conductivity, wedge-shaped proppant packs along the dominant flow channels and at the near-wellbore fracture mouths. Ultimately, this staged control strategy not only mitigates the limited transport distance and heterogeneity issues associated with heavy/large proppants, but also prevents the "propped fracture necking" phenomenon induced by sustained high displacement, thereby comprehensively maximizing the overall effective conductivity of the fracture network.

## CRediT authorship contribution statement

**Qiang Wang:** Writing – original draft, Resources, Methodology, Funding acquisition, Formal analysis, Conceptualization. **Yufeng Wang:** Writing – original draft, Supervision, Resources, Investigation, Formal analysis, Conceptualization. **Jinzhou Zhao:** Supervision, Project administration, Investigation, Funding acquisition. **Hai Liu:** Methodology, Formal analysis. **Hao Gao:** Visualization, Validation. **Yuchao Zhou:** Software, Data curation. **Yongquan Hu:** Writing – review & editing, Funding acquisition.

## Declaration of competing interest

The authors declare that they have no known competing financial interests or personal relationships that could have appeared to influence the work reported in this paper.

## Acknowledgement

This paper is supported by the joint project of National Natural Science Foundation of China (No. U21B2071), the key support project of National Natural Science Foundation of China (No. U23B20156), the National Natural Science Foundation of China (No. 52304041), and the Sichuan Provincial Natural Science Youth Fund (No. 2025ZNSFSC1353).

## References

Andrews, M. J., & O'Rourke, P. J. (1996). The Multi-Phase Particle-in-Cell (MP-PIC) method for dense particulate flows. *Int J Multiphase Flow, 22*(2), 379–402. https://doi.org/10.1016/0301-9322(95)00072-0

Auzerais, F. M., Jackson, R., & Russel, W. B. (1988). The resolution of shocks and the effects of compressible sediments in transient settling. *Journal of Fluid Mechanics, 195* (1), 437–462. https://doi.org/10.1017/S0022112088002472

Bahri, A., & Miskimins, J. (2021). The effects of fluid viscosity and density on proppant transport in complex slot systems. *SPE Prod & Oper, 36*(4), 894–911. https://doi.org/10.2118/204175-PA. SPE-204175-PA.

Clark, P. E., & Guler, N. (1983). Prop transport in vertical fractures: Settling velocity correlations. In *SPE-11636-MS, paper presented at the SPE/DOE low permeability gas reservoirs symposium*. https://doi.org/10.2118/11636-MS. Denver, Colorado, March. SPE/DOE 11636.

Cleary, M. P., Johnson, D. E., Kogsbøll, H-H., Owens, K. A., Perry, K. F., de Pater, Stachel, A., Schmidt, H., & Tambini, M. (1993). Field implementation of proppant slugs to avoid premature screen-out of hydraulic fractures with adequate proppant concentration. In *Paper presented at the low permeability reservoirs symposium*. https://doi.org/10.2118/25892-MS. Denver, Colorado.

Daniel, F., & Ingrid, T. (2019). Experimental investigation of sand proppant particles flow and transport regimes through narrow slots. *Powder Technology, 343*, 495–511. https://doi.org/10.1016/j.powtec.2018.11.004

Denney, D. (2010). Proppant transport in slickwater fracturing of shale gas for-mations. *Journal of Petroleum Technology, 62*(10), 56–59. https://doi.org/10.2118/1010-0056-JPT

Gong, F., Babadagli, T., Huang, H., & Li, H. (2024). Resolved CFD-DEM simulation of proppant aggregating and bridging mechanisms in a narrowing fracture. *Powder Technology, 437*, Article 119548. https://doi.org/10.1016/j.powtec.2024.119548

Gong, Y., Mehana, M., El-Monier, I., & Viswanathan, H (2020). Proppant placement in complex fracture geometries: A computational fluid dynamics study. *Journal of Natural Gas Science and Engineering, 79*, Article 103295. https://doi.org/10.1016/j.jngse.2020.103295

Han, J., Wang, J. Y., & Puri, V. (2016). A fully coupled geomechanics and fluid flow model for proppant pack failure and fracture conductivity damage analysis. *Journal of Natural Gas Science and Engineering, 31*, 546–554. https://doi.org/10.1016/j.jngse.2016.03.034

Han, J., Yuan, P., Huang, X., Zhang, H., Sookprasong, A., Li, C., & Dai, Y. (2016). Numerical Study of proppant transport in complex fracture geometry. In *Paper presented at the SPE Low Perm Symposium, Denver, Colorado, USA, May*, 10.2118/180243-MS. SPE-180243-MS.

Harris, S. E., & Crighton, D. G. (1994). Solitons, Solitary waves, and voidage disturbances in gas-fluidized beds. *Journal of Fluid Mechanics, 266*, 243–276. https://doi.org/10.1017/S0022112094000996

He, X., Li, W., Dang, L., Huang, S., Wang, X., Zhang, C., Zhang, N., & Chen, Y. (2021). Key technological challenges and research directions of deep shale gas development. *Natural Gas Industry, 41*(1), 118–124. https://doi.org/10.3787/j.issn.1000-0976.2021.01.010

Hou, L., Cheng, Y., Wang, X., Ren, J., & Geng, X. (2022). Effect of slickwater-alternate-slurry injection on proppant transport at field scales: A hybrid approach combining experiments and deep learning. *Energy, 242*, Article 122987. https://doi.org/10.1016/j.energy.2021.122987

Hu, Y., Wang, Y., Wang, Q., Zhao, J., Zhu, J., Li, X., & Yang, Y. (2025). The propagation laws of hydraulic fractures under the influence of natural fracture zones. *Physics of Fluids, 37*(1), Article 016616. https://doi.org/10.1063/5.0244800

Hu, Y., Wang, Q., Zhao, J., Chen, S., Li, D., Xu, R., & Zhao, C. (2021). Numerical simulation of complex fracture geometry caused by hydrodynamics in shale with pre-existing weak planes. *Journal of Petroleum Science and Engineering, 199*, Article 108306. https://doi.org/10.1016/j.petrol.2020.108306

Hu, X., Wu, K., Song, X., Yu, W., Tang, J., Li, G., & Shen, Z. (2018). A new model for simulating particle transport in a low-viscosity fluid for fluid-driven fracturing. *AIChE Journal, 64*(9), 3542–3552. https://doi.org/10.1002/aic.16183

Kong, X., & McAndrew, J. (2017). A computational fluid dynamics Study of proppant placement in hydraulic Fracture networks. In *Paper presented at the SPE Unconventional Resources Conference*. https://doi.org/10.2118/185083-MS. Calgary, Alberta, Canada, February. SPE-185083-MS.

Li, J. (2024). Computational fluid dynamics-discrete element method modeling and analysis of proppant transportation inside different degrees of inclined tortuous hydraulic fractures. *SPE Journal, 29*(1), 260–276. https://doi.org/10.2118/217461-PA

Li, J., Kuang, S., Huang, F., & Liu, P. (2024). CFD-DEM approach to Study the proppant transport and placement under different perforation conditions in tortuous hydraulic fractures. *SPE Journal, 29*(1), 277–298. https://doi.org/10.2118/217472-PA

Li, N., Li, J., Zhao, L., Luo, Z., Liu, P., & Guo, Y. (2017). Laboratory testing on proppant transport in complex-fracture systems. *SPE Prod & Oper, 32*, 382–391. https://doi.org/10.2118/181822-PA

Liu, B., Kumar, D., & Ghassemi, A. (2025). Modeling proppant transport and settlement in 3D fracture networks in geothermal reservoirs. *Geothermics, 125*, Article 103176. https://doi.org/10.1016/j.geothermics.2024.103176

Ma, X., & Xie, J. (2018). The progress and prospects of shale gas exploration and exploitation in southern Sichuan Basin, NW China. *Petroleum Exploration and Development, 45*(1), 161–169. https://doi.org/10.11698/PED.2018.01.18

Mao, S., Shang, Z., Chun, S., Li, J., & Wu, K. (2019). An efficient three-dimensional multi-phase particle-in-cell model for proppant transport in the field Scale. In *Paper presented at the SPE/AAPG/SEG unconventional resources technology conference, Denver, Colorado, USA*, 10.15530/urtec-2019-462. 22–24 July. URTEC-2019-462-MS.

Mao, S., Zhang, Z., Chun, T., & Wu, K. (2021). Field-Scale numerical investigation of proppant transport among multicluster hydraulic fractures. *SPE Journal, 26*(1), 307–323. https://doi.org/10.2118/203834-PA

Nilzon, A., & Hu, X. (2023). Numerical simulation of proppant transport in complex fracture network. In *Paper presented at the SPE Argentina exploration and production of unconventional resources symposium, Buenos Aires, Argentina*. https://doi.org/10.2118/212713-MS, 20 – 22 March. SPE-212713-MS.

O'Rourke, P. J., & Snider, D. M. (2010). An improved collision damping time for MP-PIC calculations of dense particle flows with applications to polydisperse sedimenting beds and colliding particle jets. *Chem Eng Sci, 65*(22), 6014–6028. https://doi.org/10.1016/j.ces.2010.08.032

Patankar, N. A., & Joseph, D. D. (2001). Lagrangian numerical simulation of particulate flows. *Int J Multiphase Flow, 27*(10), 1685–1706. https://doi.org/10.1016/S0301-9322(01)00025-8

Qu, H., Liu, Y., Zeng, S., Xiao, H., Lu, Y., & Liu, Z. (2022). Effect of natural fracture characteristics on proppant transport and placement in an irregular, nonplanar fracture. *SPE Journal, 27*, 2208–2225. https://doi.org/10.2118/209619-PA

Qu, H., Tang, S., Liu, Z., Mclennan, J., & Wang, R. (2021). Experimental investigation of proppant particles transport in a tortuous fracture. *Powder Technology, 382*, 95–106.

Roostaei, M., Nouri, A., Fattahpour, V., & Chan, D. (2018). Numerical simulation of proppant transport in hydraulic fractures. *Journal of Petroleum Science and Engineering, 163*, 119–138. https://doi.org/10.1016/j.petrol.2017.11.044

Sahai, R., Miskimins, J. L., & Olson, K. E. (2014). Laboratory results of proppant transport in complex fracture systems. In *Paper presented at the hydraulic fracturing technology conference*. https://doi.org/10.2118/168579-MS. The Woodlands, Texas, USA, 4-6 February,. SPE-168579-MS.

Siddhamshetty, P., Mao, S., Wu, K., & Kwon, J. S. I. (2020). Multi-Size proppant pumping schedule of hydraulic fracturing: Application to a MP-PIC model of unconventional reservoir for enhanced gas production. *Processes, 8*(5), 570. https://doi.org/10.3390/pr8050570

Snider, D. M. (2001). An incompressible three-dimensional multiphase particle-in-cell model for dense particle flows. *Journal of Computational Physics, 170*(2), 523–549. https://doi.org/10.1006/jcph.2001.6747

Tatman, G., Bahri, A., Zhu, D., Hill, A. D., & Miskimins, J. L. (2022). Experimental Study of proppant transport using 3d-Printed rough fracture surfaces. In *aper presented at the SPE annual technical conference and exhibition*, 10.2118/210196-MS. Houston, Texas, USA, October. SPE-210196-MS.

Tong, S., & Mohanty, K. K. (2016). 2016 Proppant transport study in fractures with intersections. *Fuel, 181*(1), 463–477. https://doi.org/10.1016/j.fuel.2016.04.144

Tsai, K., Fonseca, E., Degaleesan, S., & Lake, E. (2013). Advanced computational modeling of proppant settling in water fractures for shale gas production. *SPE Journal, 18*(1), 50–56, 10.2118/151607-PA. SPE-151607-PA.

Wang, Y., Liu, H., Hu, X., Dai, C., & Fang, S. (2024b). Fracture network types revealed by well test curves for Shale Reservoirs in the Sichuan Basin, China. *Energy Geoscience, 5*(1), Article 100135. https://doi.org/10.1016/j.engeos.2022.09.005

Wang, Q., Wang, Y., Sun, Y., Zhao, J., Hu, Y., Song, Y., & Du, Y. (2025). The law of zipper fracturing fracture propagation in deep shale gas wells under the influence of small faults. *Natural Gas Geoscience, 36*(2), 342–353. https://doi.org/10.11764/j.issn.1672-1926.2024.07.008

Wang, Q., Yang, Y., Zhao, J., Zhuang, W., Xu, Y., Hou, J., Zhang, Y., Hu, Y., Wang, Y., & Li, X. (2026). Simulation of proppant transport in complex fracture networks based on the multiphase particle-in-cell method. *Petroleum Exploration and Development, 53*(1), 213–222. https://doi.org/10.1016/S1876-3804(26)60688-X

Wen, C. Y., & Yu, Y. H. (1966). Mechanics of fluidization. In *Chemical engineering progress symposium series* (Vol. 62, pp. 100–111). New York, New York, USA: American Institute of Chemical Engineers.

Williams, F. A. (2018). *Combustion theory*. Boca Raton, Florida, USA: CRC Press.

Wang, Q., Wang, Y., Hu, Y., Zhao, J., Song, Y., & Shen, C. (2024a). The law of fracture propagation and intersection in zipper fracturing of deep shale gas wells. *Petroleum Exploration and Development, 51*(5), 1316–1326. https://doi.org/10.1016/S1876-3804(25)60543-X

Xiao, H., Li, Z., He, S., Lu, X., Liu, P., & Li, J. (2021). Experimental study on proppant diversion transportation and multi-size proppant distribution in complex fracture networks. *Journal of Petroleum Science and Engineering, 196*, Article 107800. https://doi.org/10.1016/j.petrol.2020.107800

Yang, R., Guo, J., Zhang, T., Zhang, X., Ma, J., & Li, Y. (2019). Numerical Study on proppant transport and placement in complex fractures System of shale Formation using eulerian multiphase model approach. In *Paper presented at the international petroleum technology conference, Beijing, China* (pp. 26–28). https://doi.org/10.2523/IPTC-19090-MS. March. IPTC-19090-MS.

Yang, C., Ma, C., Yang, Z., Wang, H., Qu, J., Yi, L., Yi, D., & Li, Y. (2025). Numerical simulation of proppant transport in dynamic fracture networks using Eulerian-Eulerian method. *Engineering Fracture Mechanics, 324*, Article 111264. https://doi.org/10.1016/j.engfracmech.2025.111264

Yao, S., Chang, C., Hai, K., Huang, H., & Li, H. (2022). A review of experimental studies on the proppant settling in hydraulic fractures. *Journal of Petroleum Science & Engineering, 208*, Article 109211. https://doi.org/10.1016/j.petrol.2021.109211

Yu, H., Taleghani, A. D., & Lian, Z. (2019). On how pumping hesitations may improve complexity of hydraulic fractures, a simulation study. *Fuel, 249*, 294–308. https://doi.org/10.1016/j.fuel.2019.02.105

Zeng, B., Bai, Y., Song, Y., Guo, X., Zhou, X., Huang, H., Shen, C., Hu, X., & Zhou, F. (2022). Proppant transport in main-secondary-tertiary fracture System in shale reservoirs. In *Paper presented at the unconventional resources technology conference*, 10.15530/urtec-2022-3722495. Houston, Texas, USA, 20-22 June.

Zeng, J., Li, H., & Zhang, D. (2019). Numerical simulation of proppant transport in propagating fractures with the multi-phase particle-in-cell method. *Fuel, 245*, 316–335. https://doi.org/10.1016/j.fuel.2019.02.056

Zhang, B., Gamage, R. P., Kong, L., & Zhang, C. (2025). Cross-scale proppants transport in the shale hydraulic fracture network: A hybrid CFD-DEM investigation. *Engineering Geology, 354*, Article 108160. https://doi.org/10.1016/j.enggeo.2025.108160

Zhang, T., Guo, J., & Liu, W. (2014). CFD simulation of proppant Transp ortation and settling in water fracture treatments. *Journal of Southwest Petroleum University: Science & Technology Edition, 36*(1), 74–82. DOI: 10.1.1.885/j.issn.1674-5086.2013.1.1.07.06.

Zhao, J., Yong, R., Hu, D., She, C., Fu, Y., Wu, J., Jiang, T., Ren, L., Zhou, B., & Lin, R. (2024). Deep and ultra-deep shale gas fracturing in China: Problems, challenges and directions. *Acta Petrolei Sinica, 45*(1), 295–311. https://doi.org/10.7623/syxb202401017

Zhao, K., Wang, J., Xu, H., & Jiang, H. (2024). Numerical simulation Study of proppant migration and settlement behavior in complex fractures. In *Paper presented at the 58th US Rock Mechanics/Geomechanics Symposium* (pp. 24–736). Golden, Colorado, USA: ARMA. 10.56952/ARMA-2024-0736. 23-26 June.

Zhou, Y. (2026). Multi-source and multi-attribute collaborative fracture network modeling of a sandstone reservoir in Ordos Basin. *Energy Geoscience, 7*(1), Article 100462. https://doi.org/10.1016/j.engeos.2025.100462

Zhou, H., Guo, J., Zhang, T., Guo, H., Chen, C., Wang, S., & Tang, T. (2023). Numerical study of the wall-retardation effect on proppant transport in rough fractures. *Computers and Geotechnics, 159*, Article 105425. https://doi.org/10.1016/j.compgeo.2023.105425

Zhou, M., Yang, Z., Xu, Z., Song, X., Wang, B., Zheng, Y., Zhou, Q., & Li, G. (2024). CFD-DEM modeling and analysis study of proppant transport in rough fracture. *Powder Technology, 436*, 119461. https://doi.org/10.1016/j.powtec.2024.119461